PSFC/JA-21-116

Evidence for Suprathermal Ion Distribution in Burning Plasmas

E. P. Hartouni,[1], A. S. Moore,[1], A. J. Crilly,[2], B. D. Appelbe,[2] P. A. Amendt,[1] K. L. Baker,[1] D. T. Casey,[1] D. S. Clark,[1] T. Doppner,[1] M. J. Eckart,[1] J. E. Field,[1] M. Gatu-Johnson,[3] G. P. Grim,[1] R. Hatarik,[1] J. Jeet,[1] S. M. Kerr,[1] J. Kilkenny,[4] A. L. Kritcher,[1] K. D. Meaney,[5] J. L. Milovich,[1] D. H. Munro,[1] R. C. Nora,[1] A. E. Pak,[1] J. E. Ralph,[1] H. F. Robey,[1] J. S. Ross,[1] D. J. Schlossberg,[1] S. M. Sepke,[1] B. K. Spears,[1] C. V. Young,[1] and A. B. Zylstra[1]

[1]Lawrence Livermore National Laboratory, Livermore, California 94550, USA
[2]Centre for Inertial Fusion Studies, The Blackett Laboratory, Imperial College, London SW7 2AZ, United Kingdom
[3]Massachusetts Institute of Technology, Plasma Science and Fusion centre, Cambridge, MA 02139, USA
[4]General Atomics, San Diego, California 92121, USA
[5]Los Alamos National Laboratory, Los Alamos, New Mexico, 87545, USA

June 2021

Plasma Science and Fusion Center
Massachusetts Institute of Technology
Cambridge MA 02139 USA

Livermore National Laboratory is operated by Lawrence Livermore National Security for the US Department of Energy, National Nuclear Security Administration, under contract no. DE-AC52-07NA27344. This Article (LLNL-JRNL-824268) was prepared as an account of work sponsored by an agency of the US government. The MIT portion of the work was supported by LLNL under contract number B640112.

Submitted to *Nature Physics*

Evidence for suprathermal ion distribution in burning plasmas

E. P. Hartouni,[1, a)] A. S. Moore,[1, b)] A. J. Crilly,[2, c)] B. D. Appelbe,[2] P. A. Amendt,[1] K. L. Baker,[1] D. T. Casey,[1] D. S. Clark,[1] T. Döppner,[1] M. J. Eckart,[1] J. E. Field,[1, d)] M. Gatu-Johnson,[3] G. P. Grim,[1] R. Hatarik,[1] J. Jeet,[1] S. M. Kerr,[1] J. Kilkenny,[4] A. L. Kritcher,[1] K. D. Meaney,[5] J. L. Milovich,[1] D. H. Munro,[1, e)] R. C. Nora,[1] A. E. Pak,[1] J. E. Ralph,[1] H. F. Robey,[1] J. S. Ross,[1] D. J. Schlossberg,[1] S. M. Sepke,[1] B. K. Spears,[1] C. V. Young,[1] and A. B. Zylstra[1]

[1)] *Lawrence Livermore National Laboratory, Livermore, California 94550, USA*

[2)] *Centre for Inertial Fusion Studies, The Blackett Laboratory, Imperial College, London SW7 2AZ, United Kingdom*

[3)] *Massachusetts Institute of Technology, Plasma Science and Fusion centre, Cambridge, MA 02139, USA*

[4)] *General Atomics, San Diego, California 92121, USA*

[5)] *Los Alamos National Laboratory, Los Alamos, New Mexico, 87545, USA*

ABSTRACT

At the National Ignition Facility, inertial confinement fusion experiments aim to burn and ignite a hydrogen plasma to generate a net source of energy through the fusion of deuterium and tritium ions. The energy deposited by α-particles released from the deuterium-tritium fusion reaction plays the central role in heating the fuel to achieve a sustained thermonuclear burn. In the hydrodynamic picture, α-heating increases the temperature of the plasma, leading to increased reactivity because the mean ion kinetic energy increases. Therefore, the ion temperature is related to the mean ion kinetic energy. Here we use the moments of the neutron spectrum to study the relationship between the ion temperature (measured by the variance in the neutron kinetic energy spectrum) and the ion mean kinetic energy (measured by the shift in the mean neutron energy). We observe a departure from the relationship expected for plasmas where the ion relative kinetic energy distribution is Maxwell-Boltzmann, when the plasma begins to burn. Understanding the cause of this departure from hydrodynamic behaviour could be important for achieving robust and reproducible ignition.

EDITOR'S SUMMARY

Inertial confinement fusion experiments reveal a departure from the expected hydrodynamic behaviour of a plasma when the fusion reactions become the primary source of plasma heating.

[a)] Electronic mail: hartouni1@llnl.gov

[b)] Electronic mail: moore212@llnl.gov

[c)] Electronic mail: a.crilly16@imperial.ac.uk

[d)] On leave at P.O. Box 4076, Dorrington, Ca. 95223

[e)] retired

MAIN

Laser Indirect Drive Inertial Confinement Fusion (LID-ICF) on the National Ignition Facility (NIF) uses a hohlraum to convert laser energy into X-rays that symmetrically implode a capsule loaded with deuterium-tritium (DT) fuel Fig. 1(a). Lasers enter the top and bottom of the Au or depleted uranium (DU) hohlraum heating it with approximately 2MJ of laser energy and irradiating the capsule with approximately 200kJ of x-rays from a 300eV x-ray spectrum. This ablates the layer of material (for the capsules considered here, high-density carbon, HDC) surrounding a DT-ice layer accelerating the capsule shell up to about 380 to 390km/s. This results in compression of the DT-ice and the generation of a hot-spot plasma through PdV work on the DT gas that fills the centre of the capsule[1]. Fusion reactions ($D + T \rightarrow \alpha + n + 17.59MeV$) begin to occur in the hot-spot plasma as this is compressed and heated to ≈4-5keV. Once a sufficient flux of α (^{4}He) particles is generated by the fusion reactions, the surrounding dense DT fuel is heated by the energy loss of the α particles leaving the central core leading to "run-away" heating which ignites the fuel, shown schematically in Fig. 1(b). The details of the α particle energy deposition as it is transported through the plasma and into the fuel are important for achieving the burning-plasma regime, the condition in which this α energy exceeds the energy of the hot-spot.[2] The dominance of the α heating process, leading to the generation of a burning plasma, has been recently reported[3,4] for two shot campaigns at NIF.

Since the α particles generated in the fusion reaction are stopped by the dense fuel surrounding the hot-spot and do not escape the implosion, key physics performance parameters are determined by measuring the spectrum of escaping neutrons. On NIF these measurements, such as the implosion neutron yield (equivalent to the energy released), ion temperature, cold-fuel neutron opacity (the down-scatter ratio) and capsule velocity are made by five neutron spectrometers that view the implosion from different directions. Fig. 1(c) provides an example of a neutron and gamma arrival time spectrum in a Quartz Cherenkov Detector (QCD).

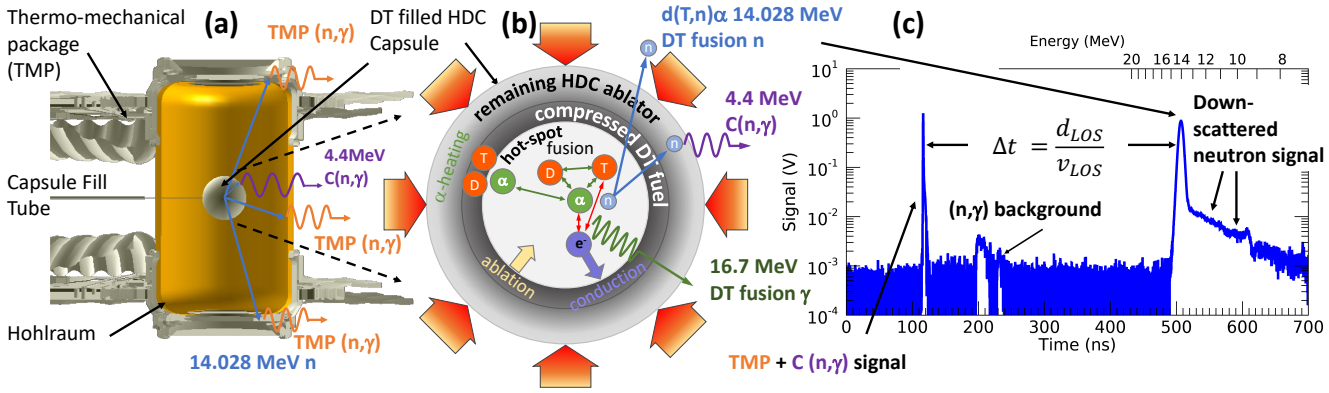

FIG. 1. Laser Indirect Drive Inertial Confinement Fusion (LID-ICF) converts laser energy into x-rays that irradiate a spherical capsule to compress and heat DT fuel to generate fusion reactions. The high density carbon capsule is filled with DT gas through a fill-tube and cryogenically frozen to create a solid DT ice layer on the inside surface. Upon heating and compression fusion of DT ions generate 14.028MeV neutrons (blue) and γ rays emitted both by the fusion reaction and by (n,γ) reactions in the surrounding capsule (purple) and target thermo-mechanical package (TMP) (orange). If heating of the compressed DT-ice fuel (b) by α particles (green) emitted by the fusion reaction exceed radiation and electron conduction losses the hot-spot reaction can become self-sustaining. The quartz Cherenkov detector neutron time-of-flight detectors on NIF uniquely measure both the γ and neutron signals at approximately 100 and 500ns (c). Low n,γ) backgrounds help enable a high precision measure of the mean line-of-sight neutron velocity $v_{\rm LOS}$ for a detector at distance $d_{\rm LOS}$.

Hydrodynamic models describing the implosions approximate the transport the α particles through the burning plasma and the cold fuel by diffusion, assuming that the α mean free path is short compared to the size of the burning region. In this approximation the plasma is in local thermal equillibrium where the ion velocity distribution is described by a Maxwellian with temperature $T_{\rm ion}$, and a relationship exists between $T_{\rm ion}$ and the mean relative kinetic energy of the ions undergoing fusion, $\bar{K}$, described by:[5–8]

$$\bar{K} = \frac{\int dK\ K^2\sigma(K)e^{-K/T_{\rm ion}}}{\int dK\ K\sigma(K)e^{-K/T_{\rm ion}}} \qquad (1)$$

where $\sigma(K)$ is the fusion cross section and $e^{-K/T_{\rm ion}}$ is the Maxwell-Boltzmann distribution. The general solution to equation 1 was described by Brysk, Ballabio and Munro for different approximations which we summarize here as:

$$\bar{K} \to T_{\rm ion}\left[\left(\frac{T_G}{T_{\rm ion}}\right)^{1/3} + \mathcal{F}(T_{\rm ion})\right] \qquad (2)$$

with $T_G = 295.5$keV for DT fusion. $\mathcal{F}(T_{\rm ion})$ is calculated using the DT fusion cross-section (see Methods)

Equation 2 has the physical interpretation that the ions with the highest likelihood of undergoing fusion occupy the tail of the Maxwell-Boltzmann distribution, e.g. for a $T_{\rm ion} = 4$keV thermal plasma, $\bar{K} \sim 5T_{\rm ion}$ and is referred to as the "Gamow" energy, first identified by Gamow[9]. At $T_{\rm ion} = 4$keV this is 5 e-foldings down from the distribution's maximum value.

The characteristics of the DT ion distribution are encoded by the neutrons generated by the fusion reactions in the plasma enabling the determination of the plasma ion kinetic energy, ion temperature and plasma velocity moments from the neutron spectral moment. For the mean neutron energy:

$$\langle E_n\rangle \approx 14.02839\text{MeV} + 0.00056\left[\langle u_\parallel\rangle + v_{\rm iso}\right] \qquad (3)$$

where the velocities are in units of km/s, and the "isotropic velocity" is defined by:

$$v_{\rm iso}(T_{\rm ion}) = 1.4641\bar{K}(T_{\rm ion}) + 0.37969T_{\rm ion} \qquad (4)$$

in which $\bar{K}(T_{\rm ion})$ and $T_{\rm ion}$ are in units of keV, and the numeric coefficients are defined by the DT cross section and Maxwellian ion distribution. The ion temperature is typically determined from the second central moment or variance of the neutron spectrum:

$$\text{Var}(E_n) \approx 0.31401\text{Var}(u_\parallel) + 6024.6\langle T_{\rm ion}\rangle \qquad (5)$$

The symbol $\langle\cdot\rangle$ represents the burn-average over the space and time moment of the plasma variables. $u_\parallel$ is the projection of the plasma velocity along a particular direction (e.g. the line-of-sight from the target to spectrometer). The isotropic velocity is the manifestation of the neutron energy upshift due to two physical factors: (1) additional relative velocity of the D and T ions in their centre-of-mass frame leading the first term in equation 4, and (2) the motion of the the centre-of-mass frame which is related to the ion temperature and leads to the second term. A description of how the velocity and temperature is determined from the diagnostics appears in the Methods section.

Taking advantage of the relationship between the mean ion kinetic energy and the ion temperature, in a thermal plasma a sufficiently precise determination of the

isotropic velocity, equations 2 and 4, would provide a measure of the ion temperature[10] independent from the plasma velocity variance in equation 5; we note that treating the neutron kinematics relativistically is essential in achieving this accuracy. The thermal or hydrodynamic expectation is then simply equation 4.

Equation 5 anticipates a source of neutron kinetic energy variance in addition to the average ion temperature. This term is due to the ion velocity variance as viewed along a line-of-sight that may result from flows generated inside the hot-spot due to asymmetries in the implosion. The anisotropic component of this velocity variance appears as an anisotropic "apparent $T_{\rm ion}$" measured by the neutron diagnostics, denoted T_{ion} in table I. The ion velocity variance could also contain radial components which would appear the same in all directions and increase the apparent $T_{\rm ion}$ measurement. This was observed by Jarrott et al. in a study comparing the apparent $T_{\rm ion}$ with the emissivity-weighted electron temperature in which the neutron measurement over predicts the electron temperature by 100s of eV[11].

The largest systematic uncertainty in the apparent $T_{\rm ion}$ measurement comes from uncertainties in the instrument response function.[12] Lacking an ion temperature calibration source, the instrument response function is built from data (obtained in "timing shots," intense and instantaneous pulses of gamma radiation, and in exploding pushers for which the long time tail of the signals are known to be free from the primary neutron scatter).The magnitude of this uncertainty is estimated to be 240eV.

On each neutron yield shot a suite of analysis codes are run to produce a set of scaler metrics for the shot. These scalers are then used to produce three dimensional values, such as $\vec{v}_{\rm HS}$, and scaler quantities averaged over multiple line-of-sight measurements such as $v_{\rm iso}$ and $T_{\rm ion}$. Relationships like equation 1 can be used to assess the state of the plasma during the burn duration. Fig. 2 shows the data for implosions using a high density carbon ablator (HDC) with a cryogenic layer of solid DT and a central DT vapor . The laser pulse wave-forms and the hohlraum dimensions change within this data set.

Fig. 2 shows that most of the low yield implosions at NIF (circles) are within systematic uncertainty to the expectation of a plasma described by a single temperature Maxwellian. This region is shown below and right of the boundary indicated by equation 4 shown as the thick gray line. Ten shots are highlighted with square symbols and more detail provided in table I. The table identifies the measured $v_{\rm iso}$ and $T_{\rm ion}$, and compares these, in the rightmost columns, to two values that are calculated by equation 4. The first expectation in column 5 assumes the measured $T_{\rm ion}$ to calculate $v_{\rm iso}$, while the second in column 6 assumes the reverse and uses equation 4 to calculate the expected $T_{\rm ion}$ using the measured $v_{\rm iso}$.

2D simulations of similar implosions[13] are shown as a point cloud on Fig. 2 with the yield color coded, and using equations 5 and 4 for $T_{\rm ion}$ and $v_{\rm iso}$ respectively, including all higher moment terms. The simulation trends as it

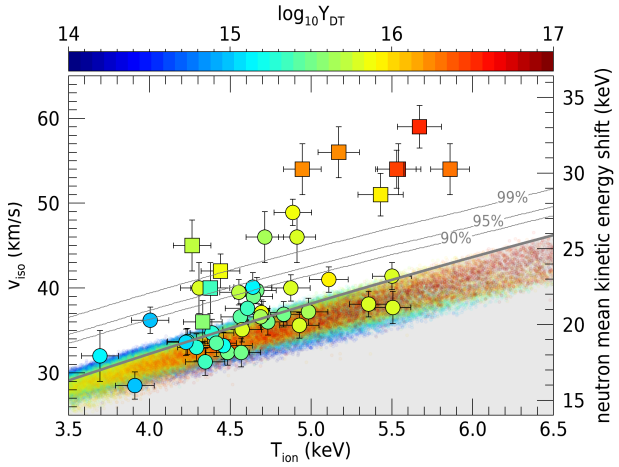

FIG. 2. The interdependence of isotropic velocity ($v_{\rm iso}$) and ion temperature ($T_{\rm ion}$). Implosions of DT ignition capsules in circles and square (square symbols represent the data in Table 1) symbols with uncertainties indicated with the neutron yield ($Y_{\rm DT}$) indicated as a color code. The high resolution 3D simulations are shown as diamonds. The boundary, equation 4 is indicated by the thick black line. If a range of ion temperatures exist in the hot-spot plasma volume and during the time neutrons are generated the result is to increase T due to the increased velocity distribution creating a "hydrodynamically accessible" region shaded gray below the boundary. The 2D simulation ensemble for similar implosions is shown as the point cloud, using equations 5 for $T_{\rm ion}$ and 4 for $v_{\rm iso}$ and color coded for yield. This point cloud is bounded by the 90%, 95% and 99% confidence interval indicating the regions of expected statistical fluctuations of an implosion described by the simulation using $\delta v_{\rm iso} = 3$km/s and $\delta T_{\rm ion} = 0.100$keV. The mean neutron energy upshift equivalent to $v_{\rm iso}$ is plotted on the right axis. Error bars include contributions from systematic and 1 standard deviation statistical uncertainties.

would for a single temperature Maxwellian displaced by the plasma velocity distribution which tends to increase the $T_{\rm ion}$. The increased $T_{\rm ion}$ results in increased yield along the ion kinetic energy boundary. The calculations represent a realistic instantiation of the hydrodynamics of these implosions and use particle monte carlo (PMC) to transport ions produced in the burn. The high-resolution 3D simulations[14] include more engineering features and drive asymmetries. These calculations simulate specific shots in the data set appearing in Fig. 2.

Confidence intervals are constructed using a gaussian likelihood calculated from the region described by the simulation data. For each "slice" of $T_{\rm ion}$ a cumulative distribution function in $v_{\rm iso}$ of the summed gaussian likelihoods provides the upper and lower limits for which the probability integrates to the confidence interval value. Of the 44 measured data points, 11 are outside of the 99% confidence interval, 8 of those belong to the HyE and I-Raum campaigns[15]. These implosions represent a departure from the behavior expected by a plasma characterized by a single ion temperature Maxwellian ion dis-

TABLE I. Neutron yield ($Y_{\rm DT}$) and ion temperature ($T_{\rm ion}$) data. Values for the implosions depicted with square symbols in Fig. 2 and the examples shown in Fig. 4 are shown in the first two columns. $v_{\rm iso}(T)$ is the expected isotropic velocity[8] calculated from the nominal experimental value $T_{\rm ion}$. The column labeled $T(v_{\rm iso})$ calculates the ion temperature for a Maxwell-Boltzmann plasma with the observed $v_{\rm iso}$. 1 sigma error bars for the measured $v_{\rm iso}$ and $T_{\rm ion}$ have not been propagated to their respective $T(v_{\rm iso})$ and $v_{\rm iso}(T)$.

Shot ID	$v_{\rm iso}$ km/s	$Y_{\rm DT}$ 10^{16} neutrons	$T_{\rm ion}$ keV	$v_{\rm iso}(T)$ km/s	$T(v_{\rm iso})$ keV
N210207-002	59 ± 2	5.29 ± 0.16	5.67 ± 0.14	42	9.03
N201122-002	56 ± 3	3.21 ± 0.10	5.17 ± 0.13	39	8.31
N210605-001	54 ± 3	4.11 ± 0.13	5.86 ± 0.12	43	7.86
N210220-001	54 ± 3	4.99 ± 0.13	5.54 ± 0.14	41	7.86
N210307-004	54 ± 2	4.40 ± 0.14	5.53 ± 0.12	41	7.86
N201101-001	54 ± 3	3.04 ± 0.08	4.95 ± 0.12	38	7.86
N210328-001	51 ± 2	1.93 ± 0.05	5.43 ± 0.14	41	7.21
N210117-002	45 ± 3	1.40 ± 0.05	4.26 ± 0.12	34	6.01
N180930-001	41 ± 2	1.53 ± 0.04	5.50 ± 0.12	41	5.34
N201011-001	40 ± 3	0.84 ± 0.03	4.38 ± 0.12	35	5.09
N180429-001	38 ± 2	0.83 ± 0.03	4.61 ± 0.14	36	4.67
N210418-003	36 ± 2	1.06 ± 0.03	4.33 ± 0.12	34	4.40

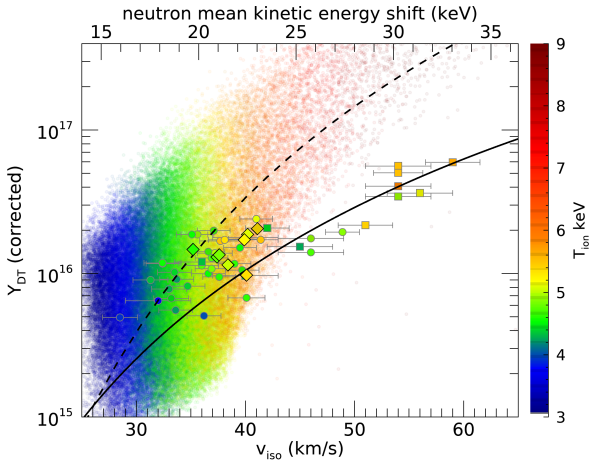

FIG. 3. The relation between measured neutron yield ($Y_{\rm DT}$) and isotropic velocity ($v_{\rm iso}$). This demonstrates that the data is burning at a cooler temperature than expected from the simulations. The upper ordinate axis translates the measured $v_{\rm iso}$ into the kinetic energy upshift (ΔE) that it represents in the centre -of-mass frame of the DT fusion reaction. Experimental data points are shown as circles and squares the shots in Table I are depicted as squares. The 2D simulation ensemble for similar implosions is shown as the point cloud, using equation 4 for $v_{\rm iso}$ and the calculated yield. High-resolution 3D simulations are shown as diamonds. The experimental neutron yield and the 3D simulations are corrected to account for neutron scatter off of the compressed fuel shell (see Methods). The solid line is the Maxwellian reactivity $\langle\bar{\sigma\nu}\rangle$ calculated using $T_{\rm ion}$ derived from $v_{\rm iso}$ (see Eqn. 4) and freely scaled to overlay the data. The dashed line is equivalent but using a 2.5x higher ion temperature and freely scaled to overlay the data below the hydrodynamic boundary and 2D simulations. Error bars for neutron yield and $v_{\rm iso}$ include systematic and 1 standard deviation statistical uncertainties.

tribution.

The neutron yield corrected for elastic scattering in the compressed DT fuel[16] ($Y_{\rm DT}$) for these shots is plotted against the observed $v_{\rm iso}$ in Fig. 3 (square and circular data points) and compared to the equivalent from 2D simulations (point could). Both are compared to the DT Maxwellian reactivity $\langle\bar{\sigma\nu}\rangle$ calculated using the $T_{\rm ion}$ derived from the observed $v_{\rm iso}$. The solid line is scaled in the ordinate to best fit the data. To best match the simulations, the dashed line in Fig. 3 is not only scaled in the ordinate, but must be calculated using a $T_{\rm ion}$ 2.5 times greater than derived from $v_{\rm iso}$. It is evident from this plot that the data is burning "cooler" than the simulation for a given yield. The higher apparent $T_{\rm ion}$ associated with the recent shots is consistent with an increase in the population of ion kinetic energy $\gtrsim$ 10keV. This ion population would be *suprathermal*, it does not exist as a consequence of the single temperature Maxwellian which governs the behavior of the majority of ions in the plasma for these implosions. The mean kinetic energy of the reacting ions is very sensitive to the shape of the ion kinetic energy distribution in this energy range as the DT fusion cross section is increasing rapidly. Small contributions of high energy ions can increase the reactivity and shift $\langle\bar{K}\rangle$ to higher values, however ions with energies significantly greater than thermal also start to increase Var(E_n), so this data places a unique constraint on the shape and energy of the DT ion distribution that is fusing and generating neutrons.

The upscattering of ions to higher energies through elastic collision with the fusion alpha particles can act to increase the higher energy ion population, however this is accounted for by the PMC used in the simulations. The PMC samples a subset of ions and tracks them through the plasma until a specified kinetic energy of the scattered ion is reached - at which point the calculation stops and remaining energy deposited in that cell. Changing this parameter from 100keV to 10keV increases the yield by less than 10% in 1D simulations and does not account for the increases in yield or $v_{\rm iso}$ observed in the data.

Other subtle changes to the neutron spectrum represented by skew and kurtosis, and reaction-in-flight neutrons can also move the mean neutron energy slightly but are estimated to contribute less than 1 km/s shifts in $v_{\rm iso}$. Ion distributions described with multiple Maxwellians of different ion temperatures will result in $v_{\rm iso}$ below the boundary defined by equation 4.

We summarize the possible physical causes for the observed difference from Maxwellian into four general hypotheses: (1) Kinetic, (2) Hydrodynamic, (3) Burn-temporal extent, and (4) Burn-spatial extent.

For hypothesis 1 suprathermal DT ion distributions are predicted in some models that incorporate kinetic effects in the implosions[17,18]. However, most of these published

studies of ion kinetic effects consider the hot-spot only and start with higher ion temperatures than exists in the implosions studied here[17–20]. The alpha particles produced in DT fusion are suprathermal (having 3.5MeV in a ≈ 5keV DT plasma), the majority of their kinetic energy comes from the Q (17.59 MeV) of the fusion reaction, which is much larger than the ion temperature. The details of how the alpha particles transfer their energy to the surrounding plasma, plasmas that are at the temperatures and densities of the current NIF implosions (fuel shell temperatures ∼ 1 to 2 keV, areal densities ∼ 1g/cm^2), is an open experimental question. Hypothesis 2 results from the slight neutron opacity of the hot-spot which can lead to fewer neutrons from the far-side of the hot-spot (away from the spectrometer) reaching the detector than those emitted on the near-side. This can act to upshift the mean neutron energy if the hot-spot is expanding radially, but is present in the HYDRA simulations which should show this hydrodynamic behavior. The 3rd hypothesis requires a large ($> 10\%$) early time yield (e.g. from the shock convergence in the capsule), shifting the mean of the total neutron time-of-flight distribution early generating an apparent isotropic velocity. Hypothesis 4 requires the neutron burn region separated from the presumed capsule centre of order 10 mm, and is ruled out by neutron images.

Two examples of how different suprathermal distribution (hypothesis 1) can change the values of $v_{\rm iso}$ and $T_{\rm ion}$ are shown in the Methods section and illustrate that to move significantly above the Maxwellian boundary requires a more 'boxy' distribution in which a suprathermal population exists with a cut-off in energy similar to that described by Peigney et al..

Experimental, theoretical and simulation work continues to identify the cause of the observation. The departure from Maxwellian plasma behavior is a signature of this burning plasma domain.

METHODS

Determining the implosion attributes with neutron time-of-flight

Additions to the nuclear diagnostics at NIF, by the use of Cherenkov neutron time-of-flight (nToF) spectrometers and by a fifth nToF line-of-sight (LOS)[10], have improved the ability to detect implosion anisotropy through measurements of the neutron kinetic energy spectrum.[21] These high precision measurements[22] simultaneously measure both γ rays and neutrons emitted by nuclear reactions associated with only the fusion burn. Since the time-of-flight diagnostics integrate the neutron spectrum over the duration of the burn (of order 100 to 200ps), distinguishing between neutrons emitted while generating the hot-spot compared to those emitted by α heating is not possible. However, the improved precision of the nToF measurements on NIF have uncovered distinguishing signatures of the neutron spectrum that are unique to the generation of a burning plasma.

The determination of the "hot-spot velocity", the average of the velocity of the DT ion pairs undergoing fusion, provides information on the capsule drive asymmetries[23] and also on the mean of the neutron kinetic energy distribution[10]. The ion temperature is determined by a forward-fit of the neutron time-of-flight spectrum whose parameters include the variance of the neutron kinetic energy distribution.[24], which includes not only the ion temperature but also plasma velocity variance.

Multiple line-of-sight measurements of the neutron spectral moments are necessary to determine the hot-spot and the isotropic velocities. There are 6 neutron time-of-flight spectrometers line-of-sight with scintillator detectors capable of measuring the neutron kinetic energy spectrum.[24–27] Five of these lines-of-sight have an additional spectrometer system, the Quartz Cherenkov Detector (QCD)[22] optimized to have high timing precision for high yield implosions.

The QCD system measures the "γ-flash" which is used to determine the time-of-flight of photons produced during the implosion. This is measured with a precision of ±25ps. The γ-flash is created by a combination of processes as illustrated in Fig. 1: the direct DT→ ^{5}Heγ fusion channel, (n,γ) reactions on the carbon ablator that emit at 4.4MeV, and (n,γ) interactions with the Thermal-Mechanical Package (TMP), which is a part of the target system, and generates a broad spectrum of γ rays up to about 8MeV. The relatively low-energy Cherenkov threshold of the QCD system means that the signal is predominantly from the 1-5MeV γ rays emitted by the neutron reactions with the TMP and HDC ablator. Because of the finite flight time of the neutrons to these scattering source, the gammas generated from these reactions will arrive at the detector between 20 and 60ps later than the fusion gammas. The QCD also measures the arrival time of the DT neutrons to ±16ps, and the uncertainty of the 20 meter flight path ($d_{\rm LOS}$) is ±1mm. The right-hand side of Fig. 1 showing the raw data measured by the QCD nToF detectors demonstrating the high dynamic range of the γ and neutron signals used to determine $v_{\rm LOS}$. The uncertainties in both γ and neutron measurements combine to an overall line-of-sight velocity uncertainty of ±4.7km/s.

The five line-of-sight measurements using the QCD spectrometers are fit to a four-parameter velocity model[21]: $v_x, v_y, v_z, v_{\rm iso}$ where the 3-vector velocity components are associated with the mean burning plasma velocity, the "hot-spot velocity" and a fourth component being the "isotropic" velocity. The mean neutron kinetic energy shift for a particular line-of-sight from equation 3 contains the term:

$$\langle u_{\parallel} \rangle = v_{\rm LOS} \approx \vec{v}_{\rm HS} \cdot \hat{n}_{\rm LOS}$$

where $\hat{n}_{\rm LOS}$ is the direction vector of the line-of-sight.

This is illustrated in Fig. 4. The raw neutron spectra from one line of sight is shown in Fig. 4(a) and the time-

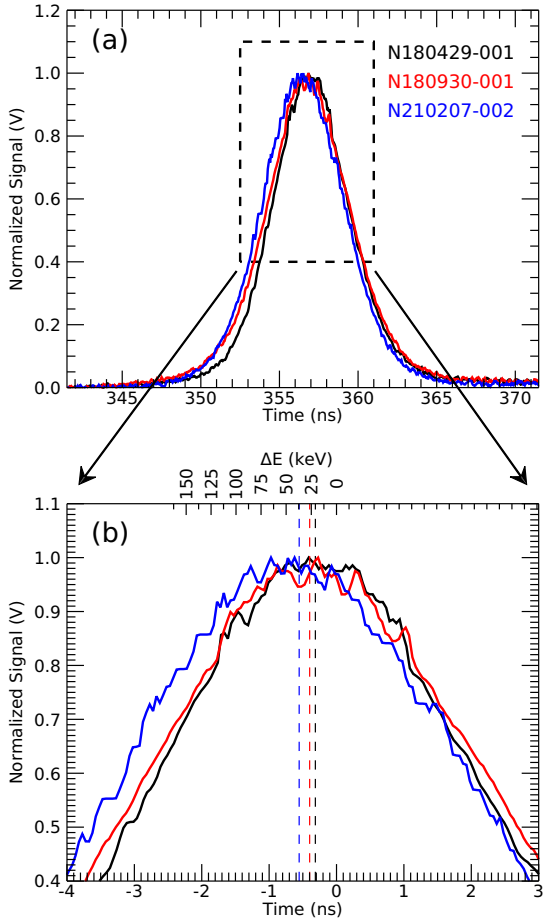

FIG. 4. Neutron spectra recorded by a single line-of-sight QCD nToF detector. The normalized data for three shots are shown to compare data from burning (N210207 - blue) and non-burning (N180429 - black, N180930 - red) implosions. In (a) the raw data from the north pole (NP) nToF is shown with the time-axis corrected to co-time the γ bang-time signals. By fitting all five nToF lines of sight the mode-1 component due to the bulk hot-spot velocity ($\vec{v}_{HS}$) can be determined and then removed for each individual line of sight ($\vec{v}_{HS} \cdot \hat{n}_{LOS}$) to reveal the different kinetic energy shifts ($\Delta E = 0.56037 v_{\rm iso}$), and the different spectral widths (Var(E_n)) as shown in (b). The mean neutron energy upshift ΔE is plotted on the upper x-axis of panel (b) for each shot and is shown as the dashed vertical line.

axis corrected to account for the approx 1ns differences in implosion bang-times for different experiments. Once the data from all lines of sight are combined, the mode-1 component can be removed as shown in Fig. 4(b). This reveals the upshift in the mean neutron energy $\Delta E = 0.56037 v_{\rm iso}$.

F(T)

The function $\mathcal{F}(T)$ is equal to 5/6 for the considerations in Brysk. In the following discussion we use the numerical results of Munro[8] (Table A.3) calculated using a relativistic expression for equation 1 and the ENDL2011 DT fusion cross section evaluation which result in:

$$\mathcal{F}(T) = \frac{0.81857 + T(0.14272 + T(-0.0048217 + 1.1536 \times 10^{-5} T))}{1 + T(-0.0027543 + T(0.0092859 + 5.1419 \times 10^{-6} T))} \quad (6)$$

Equations 3, 4 and 5 are taken from Munro's[8] equations 73 and 74 preserving only the low order terms. The coefficients are calculated using Munro's[8] Table 1 and transformed to the neutron kinetic energy, E_n (keV), coordinate system.

Neutron yield measurements

Neutron yields on NIF are measured by neutron activation of zirconium (Zr). Three Zr discs (radius = 34.9 mm and length = 7.5 mm) are positioned 4.559 m from the implosion. Neutrons emitted by the target travel to and interact with the ^{90}Zr atoms in the discs producing ^{89}Zr atoms via the (n,2n) reaction. The (n,2n) reaction cross section rises nearly linearly with energy from a threshold of 12 MeV, so the number of ^{89}Zr atoms produced is proportional to the number of DT neutrons. ^{89}Zr is unstable, and decays emitting a 909 keV γ-ray with a half-life of 78.41 hours. This half-life allows the pucks to be collected and transported to a counting facility in which the decays are energy analyzed and counted for a fixed amount of time by a dedicated Germanium detector. Accounting for the solid angle and collection efficiency of the detector this measures the number of neutrons that leave the target to an uncertainty of $1\sigma \sim 5\%$. When 14.028MeV 'primary' DT fusion neutrons generated in the hot-spot leave the target, they must pass through compressed DT fuel (see Fig. 1). The high areal density of the compressed fuel leads to significant neutron scattering in which the primary DT neutrons lose energy leading to a characteristic down-scattered tail to the neutron spectrum in addition to the primary DT fusion neutron peak. The amount of down-scatter is proportional to the compressed fuel areal density and in ICF experiments is typically characterized by the down-scatter ratio (DSR) which is the ratio of neutron yield between 10 -12 MeV and 13 - 15 MeV. The compressed fuel density changes in different experiments and so to calculate the fusion birth yield in the hot spot the measured primary neutron yield must be corrected to account for the loss due to neutron scattering. This correction factor is approximately $exp(3.8 DSR(\%)/100)$ derived from the average (n,DT) scattering cross-section (0.79b) and relation between ρr and DSR. This has been applied to the primary neutron yield (Y_n) values plotted in Fig. 3[16,28].

Impact of ion distributions on neutron spectra

The constraint of these measurements on the ion kinetic energy distribution can be assessed through calculation of neutron spectra for somewhat arbitrarily chosen, non-Maxwellian ion distribution functions[29]. Two examples are shown in Fig. 5. In Fig. 5 (a-c) a simple two-temperature Maxwell-Boltzmann ion distribution is used and the moments of the resulting neutron spectrum plotted in panel (b) and $v_{\rm iso}$ and T_{ion} calculated from the spectrum are shown in panel (c) relative to the thermal expectation (or boundary) described by equation 4. An equivalent analysis is performed for an arbitrarily chosen ion distribution function that adds a tail to a Maxwell-Boltzmann distribution in Fig. 5(d-f). The tail is described by $f_2\sqrt{E_{cut}-E}/\sqrt{E_{cut}}$. These two figures illustrate how ion distributions with significant populations with very high energy tend to increase the variance of the neutron spectrum (from which T_{ion} is derived) more quickly than the mean neutron energy associated with $v_{\rm iso}$. The alternative is true when a suprathermal population is limited to energies below a certain cut-off energy and the $v_{\rm iso}$ point lies above the thermal expectation boundary. It worth noting that this is reminiscent of the kinetic α particle energy deposition model described by Peigney et al. in which 3.5MeV α particles lose energy gradually to electrons until the reach a critical velocity at which they couple more strongly to the ion population[17].

ACKNOWLEDGMENTS

We would like to acknowledge many discussions with our colleagues: O. Landen, P. Patel, L. Divol, P. Springer and C. Cerjan.

Lawrence Livermore National Laboratory is operated by Lawrence Livermore National Security, LLC, for the U.S. Department of Energy, National Nuclear Security Administration under Contract No. DE-AC52-07NA27344. This article (LLNL-PROC-817440) was prepared as an account of work sponsored by an agency of the U.S. government. Neither the U.S. government nor Lawrence Livermore National Security, LLC, nor any of their employees make any warranty, expressed or implied, or assume any legal liability or responsibility for the accuracy, completeness, or usefulness of any information, apparatus, product, or process disclosed, or represent that its use would not infringe privately owned rights. The views and opinions of authors expressed herein do not necessarily state or reflect those of the U.S. government or Lawrence Livermore National Security, LLC, and shall not be used for advertising or product endorsement purposes.

AUTHOR CONTRIBUTIONS

E.P.H. neutron diagnostics, wrote sections of paper; A.S.M. neutron diagnostics, wrote sections of paper; A.J.C. theory; B.D.A. theory; P.A.A. hohlraum physics; K.L.B. Hybrid "Shot RI" (shot responsible individual); D.T.C. Hybrid Shot RI; D.S.C. high resolution 3D simulations, T.D. Hybrid Shot RI; M.J.E. neutron time-of-flight diagnostics; J.E.F. simulation methods; M.G.J. neutron diagnostics; G.P.G. neutron diagnostics development; R.H. neutron diagnostics development and analysis code; J.J. neutron diagnostics deployment and operations; S.M.K. neutron diagnostics deployment and operations; J.K. neutron diagnostics development; A.L.K. Hybrid-E design lead; K.D.M. gamma diagnostics; J.L.M. high resolution 3D simulations, D.H.M. theory methodology; R.C.N. post-shot simulations; A.E.P. Hybrid & I-Raum Shot RI; J.E.R. N201101 & N210207 experimentalist and Shot RI; H.F.R. original I-Raum design lead; J.S.R. I-Raum experimental lead and N201122 Shot RI; D.J.S. neutron diagnostics; S.M.S. HYDRA details; B.K.S. simulations lead; C.V.Y. present I-Raum design lead; A.B.Z. Hybrid-E experimental lead.

COMPETING INTERESTS

The authors declare no competing interests.

[1] Lindl, J., "Development of the indirect-drive approach to inertial confinement fusion and the target physics basis for ignition and gain," Physics of Plasmas **2**, 3933–4024 (1995), https://doi.org/10.1063/1.871025.

[2] Christopherson, A. R. *et al.*, "Theory of alpha heating in inertial fusion: Alpha-heating metrics and the onset of the burning-plasma regime," Physics of Plasmas **25**, 072704 (2018), https://doi.org/10.1063/1.5030337.

[3] Zylstra, A. B. *et al.*, "Burning plasma achieved in inertial fusion," Nature **601**, 542–548 (2022), https://doi.org/10.1038/s41586-021-04281-w.

[4] Kritcher, A. L. *et al.*, "Design of inertial fusion implosions reaching the burning plasma regime," Nature Physics **18**, 251–258 (2022), https://doi.org/10.1038/s41567-021-01485-9.

[5] Brysk, H., "Fusion neutron energies and spectra," Plasma Phys. **15**, 611–617 (1973), https://doi.org/10.1088/0032-1028/15/7/001.

[6] Ballabio, L., Källane, J. & Gorini, G., "Relativistic calculation of fusion product spectra for thermonuclear plasmas," Nucl. Fusion **38**, 1723–1735 (1998), https://doi.org/10.1088/0029-5515/38/11/310.

[7] Appelbe, B. & Chittenden, J., "Relativistically correct dd and dt neutron spectra," High Energy Density Physics **11**, 30–35 (2014), https://doi.org/10.1016/j.hedp.2014.01.003.

[8] Munro, D. H., "Interpreting inertial fusion neutron spectra," Nuclear Fusion **56**, 036001 (2016), https://doi.org/10.1088/0029-5515/56/3/036001.

[9] Gamow, G., "Nuclear energy sources and stellar evolution," Phys. Rev. **53**, 595–604 (1938), https://link.aps.org/doi/10.1103/PhysRev.53.595.

[10] Moore, A. S. *et al.*, "The five line-of-sight neutron time-of-flight (ntof) suite on the national ignition facility (nif)," Review of Scientific Instruments **92**, 023516 (2021), https://doi.org/10.1063/5.0040730.

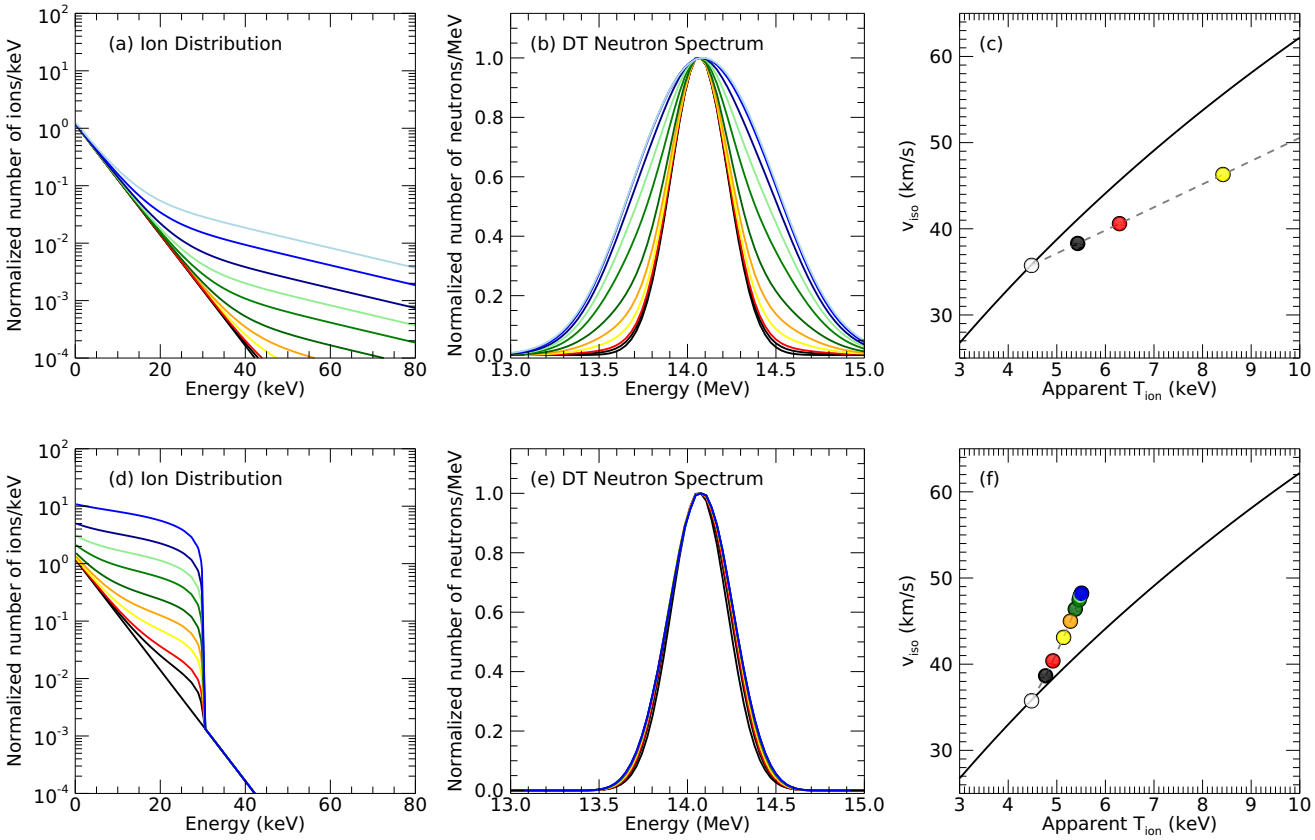

FIG. 5. Neutron spectra generated by different DT ion distribution functions. The neutron spectra in (b) and (e) are derived from the ion distribution shown in (a) and (d). (c) and (f) show the location of the $v_{\rm iso}$ and T_{ion} calculated from the spectra in (b) and (e) relative to the hydrodynamic boundary (solid line) also shown in Fig. 2. Distributions in (a) are two temperature Maxwell-Boltzmann with increasing fractions (f_2) of the higher temperature population. T_1 = 4.5keV, T_2 = 25keV, and f_2 = 0.0, 0.0004, 0.0008, 0.002, 0.004, 0.008, 0.02, 0.04, 0.08, 0.16, 0.28 . Distributions in (d) are described by a Maxwell-Boltzmann plus a tail with functional form $f_2\sqrt{E_{cut}-E}/\sqrt{E_{cut}}$ with an energy cut-off E_{cut} = 35keV and increasing fractions (f_2). T_1 = 4.5keV and f$_2$ = 0.0, 0.07, 0.13, 0.27, 0.43, 0.60, 0.79, 0.88, 0.94, 0.97. Colors represent increasing f_2 from grey, black red, yellow, orange, green, through blue. The dashed line represents the continuous locus for different fractions of the non-thermal population.

[11] Jarrott, L. C. *et al.*, "Thermal temperature measurements of inertial fusion implosions," Phys. Rev. Lett. **121**, 085001 (2018).

[12] Hatarik, R. *et al.*, "Analysis of the neutron time-of-flight spectra from inertial confinement fusion experiments," Journal of Applied Physics **118**, 184502 (2015), https://doi.org/10.1063/1.4935455.

[13] Gaffney, J. A. *et al.*, "Making inertial confinement fusion models more predictive," Physics of Plasmas **26**, 082704 (2019), https://doi.org/10.1063/1.5108667.

[14] Clark, D. S. *et al.*, "Three-dimensional modeling and hydrodynamic scaling of national ignition facility implosions," Physics of Plasmas **26**, 050601 (2019), https://doi.org/10.1063/1.5091449.

[15] Ross, J. S. *et al.*, "Experiments conducted in the burning plasma regime with inertial fusion implosions," (2021), https://arxiv.org/abs/2111.04640.

[16] Rinderknecht, H. G. *et al.*, "Azimuthal drive asymmetry in inertial confinement fusion implosions on the national ignition facility," Phys. Rev. Lett. **124**, 145002 (2020).

[17] Peigney, B. E., Larroche, O. & Tikhonchuk, V., "Ion kinetic effects on the ignition and burn of inertial confinement fusion targets: A multi-scale approach," Physics of Plasmas **21**, 122709 (2014), https://doi.org/10.1063/1.4904212.

[18] Sadler, J. D. *et al.*, "Kinetic simulations of fusion ignition with hot-spot ablator mix," Phys. Rev. E **100**, 033206 (2019), https://link.aps.org/doi/10.1103/PhysRevE.100.033206.

[19] Appelbe, B., Sherlock, M., El-Amiri, O., Walsh, C. & Chittenden, J., "Modification of classical electron transport due to collisions between electrons and fast ions," Physics of Plasmas **26**, 102704 (2019), https://doi.org/10.1063/1.5114794.

[20] Sherlock, M. & Rose, S., "The persistence of maxwellian d and t distributions during burn in inertial confinement fusion," High Energy Density Physics **5**, 27–30 (2009), https://doi.org/10.1016/j.hedp.2008.11.001.

[21] Hartouni, E. P. *et al.*, "Optimal choice of multiple line-of-sight measurements determining plasma hotspot velocity at the national ignition facility," Review of Scientific Instruments **92**, 023513 (2021), https://doi.org/10.1063/5.0040319.

[22] Moore, A. S. *et al.*, "A fused silica cherenkov radiator for high precision time-of-flight measurement of dt γ and neutron spectra (invited)," Review of Scientific Instruments **89**, 10I120 (2018), https://doi.org/10.1063/1.5039322.

[23]Spears, B. K. *et al.*, "Mode 1 drive asymmetry in inertial confinement fusion implosions on the national ignition facility," Physics of Plasmas **21**, 042702 (2014), https://doi.org/10.1063/1.4870390.
[24]Hatarik, R. *et al.*, "A new neutron Time-of-Flight detector to measure the mev neutron spectrum at the National Ignition Facility," Plasma and Fusion Research **9**, 4404104 (2014).
[25]Grim, G. P. *et al.*, "The 27.3 meter neutron time-of-flight system for the National Ignition Facility," in *Penetrating Radiation Systems and Applications XIV*, Vol. 8854, edited by Grim, G. P. & Barber, H. B., International Society for Optics and Photonics (SPIE, 2013) pp. 70–81, https://doi.org/10.1117/12.2030170.
[26]Clancy, T. J. *et al.*, "Engineering architecture of the neutron Time-of-Flight (nToF) diagnostic suite at the National Ignition Facility," in *Target Diagnostics Physics and Engineering for Inertial Confinement Fusion III*, Vol. 9211, edited by Bell, P. M. & Grim, G. P., International Society for Optics and Photonics (SPIE, 2014) p. 92110A, https://doi.org/10.1117/12.2062329.
[27]Caggiano, J. A. *et al.*, "Design of a north pole Neutron Time-of-Flight (NTOF) system at NIF," Journal of Physics: Conference Series **717**, 012087 (2016), https://doi.org/10.1088/1742-6596/717/1/012087.
[28]Meaney, K. D. *et al.*, "Total fusion yield measurements using deuterium–tritium gamma rays," Physics of Plasmas **28**, 102702 (2021), https://doi.org/10.1063/5.0055846.
[29]Crilly, A. *et al.*, "Constraints on ion velocity distributions from fusion product spectroscopy," (2022), https://arxiv.org/abs/2205.04763.

DATA AVAILABILITY

Raw data were generated at the National Ignition Facility and are not available to the general public. Derived experimental data supporting the findings of this study shown in Fig. 2 and 4, but not in Table 1 are available from the corresponding authors upon reasonable request.

CODE AVAILABILITY

The simulation codes used in this manuscript are not available to the general public.